JOURNAL OF GEOPHYSICAL RESEARCH, VOL. 101, NO. B8, PAGES 17,977–17,993, AUGUST 10, 1996

Models of ocean ridge lithospheric deformation: Dependence on crustal thickness, spreading rate, and segmentation

William J. Shaw[1] and Jian Lin

Department of Geology and Geophysics, Woods Hole Oceanographic Institution, Woods Hole, Massachusetts

Abstract. We use three-dimensional (3-D) temperature and rheology models to investigate the effects of crustal thickness and ridge segmentation on mid-ocean ridge lithospheric structure. We find that crustal thickness variations associated with focused magma accretion at a slow spreading ridge segment can cause significant along-axis gradients in crustal temperature and a "pita-pocket"-shaped weak zone in the lower crust that decouples brittle upper crust from upper mantle. In contrast, fast spreading ridge segments with little crustal thickness variation are found to be uniformly weak along axis. The overthickened crust produced by ridge-hotspot interaction alters the heat balance between magma emplacement and hydrothermal cooling, creating an extremely weak lithosphere in a steady state model. We apply a simple two-dimensional (2-D) cyclic faulting model to across-axis sections of temperature and rheological structure. Slow spreading segments are predicted to have relatively large along axis variations in fault height and spacing. In contrast, fast spreading and hotspot-affected segments are predicted to have much smaller variations in faulting styles, except in the immediate vicinity of a major transform fault. The presence or lack of a steady state axial rift valley is also predicted to depend on crustal thickness, spreading rate, and the ability of rift-bounding normal faults to propagate along axis. For fast spreading and hotspot-affected segments, the sizes of axial rift valleys are predicted to be small and may not be distinguishable from those of neovolcanic or magma-chamber-supported isostatic features. This is in contrast to most slow spreading segments, where axial rift valleys are predicted to be a dominant morphological feature. For a slow spreading segment of great length, however, the axial rift valley size is predicted to diminish toward the segment center because large faults formed at segment distal ends cannot propagate through a large decoupling zone created by locally thickened crust at the segment center.

Introduction

The mechanical strength of lithosphere is a variable of paramount significance in determining the style of oceanic and continental crustal deformation [e.g., *Zuber et al.,* 1986; *Lin and Parmentier,* 1990; *Buck*, 1988, 1993; *Forsyth,* 1992]. In a mid-ocean ridge (MOR) tectonic setting, the dependence of lithospheric structure on spreading rate explains the first-order observations of large, widely spaced faults at slow spreading ridges and small, closely spaced faults at fast spreading ridges [e.g., *Searle and Laughton*, 1981; *Macdonald*, 1982]. The spreading rate alone, however, cannot explain other systematics such as variations in faulting style (i.e., fault height, spacing, and length) along slow spreading ridges [*Shaw*, 1992; *Shaw and Lin,* 1993], diminished axial rift valleys in the centers of some slow spreading segments [*Kuo and Forsyth*, 1988; *Neumann and Forsyth*, 1993], and lack of large-scale faulting at hotspot-affected ridges [*Searle and Laughton*, 1981; *Appelgate and Shor*, 1994]. Explanation of these observations requires consideration of other variables. This paper investigates how crustal thickness variation and segmentation, in addition to spreading rate, affect MOR lithospheric deformation.

We considered two sources of oceanic crustal thickness variation from the global average of 5-6 km [*Chen*, 1992]. The first is crustal thinning toward ridge segment ends as observed in seismic refraction [e.g., *Sinha and Louden,* 1983; *Detrick et al.*, 1993; *Tolstoy et al.*, 1993] and gravity studies [e.g., *Kuo and Forsyth*, 1988; *Lin et al.,* 1990; *Blackman and Forsyth*, 1991, 1992; *Morris and Detrick*, 1991; *Detrick et al.*, 1995]. Thick crust at segment centers is attributable to focused mantle upwelling below ridge segments [*Lin et al.*, 1990]. A transition from buoyancy-dominated three-dimensional (3-D) upwelling to plate driven two-dimensional (2-D) flow [*Parmentier and Phipps Morgan,* 1990; *Lin and Phipps Morgan*, 1992; *Sparks et al.*, 1993] can explain the reduced along-axis variations in crustal thickness at fast spreading rates (Figure 1a). The second source of variation we considered is overthickened crust produced by near-ridge hotspots (Figure 1b) [*White et al.*, 1992; *Ito and Lin*, 1995a,b].

Introducing crustal thickness variations has two significant effects on MOR lithospheric structure. First, the amount of

[1]Also at MIT/WHOI Joint Program in Oceanography, Woods Hole Oceanographic Institution, Woods Hole, Massachusetts.

Paper number 96JB00949.
0148-0227/96/96JB-00949$09.00

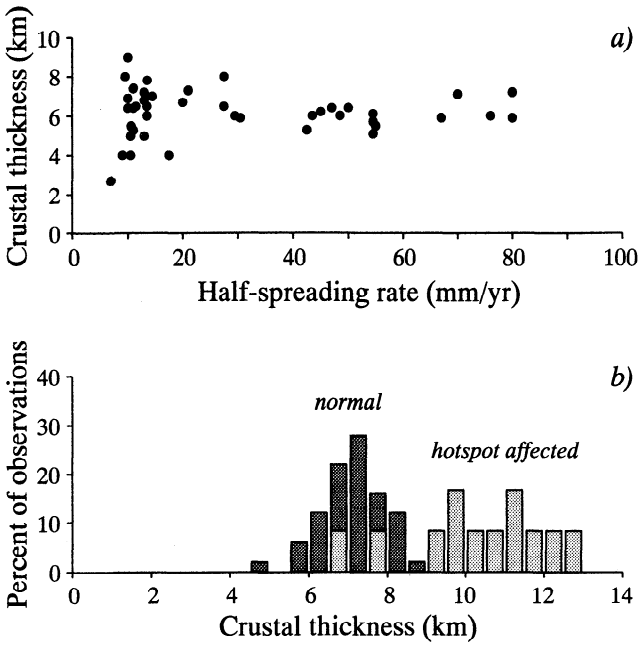

Figure 1. (a) Compilation of seismically determined oceanic crustal thickness as a function of spreading rate [from *Chen*, 1992]. (b) Histogram of oceanic crustal thickness for normal (light shading) and hotspot-affected (dark shading) crust [from *White et al.*, 1992]. Note that scatters in crustal thickness decrease with increasing spreading rate and that hotspots produce overthickened crust.

heat released from solidification of ridge-axis magma bodies is directly proportional to crustal thickness. Second, because the lower crust may be weaker than the upper mantle [e.g., *Shelton and Tullis,* 1981; *Chen and Morgan*, 1990b], variations in crustal thickness can lead to significant along-axis changes in the volume of weak lower crust.

In this paper, we first use a 3-D finite difference thermal model and crustal and mantle flow laws to predict temperature and rheological structure for a range of representative ridge configurations, focusing on the effects of along-axis crustal thickness variation and ridge segmentation. The lithospheric structure is then used as the basis for 2-D and quasi-3-D faulting models. Finally, the theoretical results are used to interpret subridge thermal structure from the observed faulting characteristics and the presence or lack of an axial rift valley.

Model Configuration

We considered five case studies that encompass a wide range of the parameter space presented by the global MOR system and for which high-resolution morphological and geophysical data are available to constrain models (Figure 2). Each model is described by a half-spreading rate u, crustal thickness t_c, lengths of ridge segments L, and the widths of associated offsets W. Prediction of crustal thickness in terms of melt production [e.g., *Phipps Morgan and Forsyth*, 1988; *Sparks et al.,* 1993; *Ito and Lin,* 1995a] is beyond the scope of this study. Instead, crustal thickness estimated from seismic and/or gravity studies of each area are used as input. Crustal magma is assumed to be emplaced in a steady state zone of finite width at the ridge axis and the imposed crustal thickness varies only along axis. For a segment of length L, mean crustal thickness $\bar{t}_c$, and amplitude of along axis variation Δt_c, the crustal thickness is described by $t_c = \bar{t}_c + \Delta t_c \cos(2\pi y/L)$, where y is the along-axis distance from the segment midpoint (Figure 2).

The north Mid-Atlantic Ridge long segment model (NMARL) simulates the first ridge segment south of the Atlantis transforms at 29°30'-30°N [*Sempéré et al.*, 1990, 1993], where a large, negative "bull's-eye"-shaped mantle Bouguer anomaly is centered at the shallowest part of the segment [*Lin et al.*, 1990]. If the residual gravity anomaly is due entirely to crustal thickness variations, *Lin et al.* [1990] calculated a roughly sinusoidal crustal thickness variation with L = 50 km, $\bar{t}_c$ = 5 km, and Δt_c = 2 km (Figure 2a). The north Mid-Atlantic Ridge short segment model (NMARS) represents a short segment bounded by small offsets near 28°50'N [*Sempéré et al.*, 1990, 1993]. Crustal thickness variations, as inferred from residual gravity, are taken to be sinusoidal with L = 25 km, $\bar{t}_c$ = 3.75 km, and Δt_c = 0.75 km [*Lin et al.*, 1990] (Figure 2b).

The well-studied segment of the MAR near 32°-34°S [*Kuo and Forsyth,* 1988; *Grindlay et al.,* 1991; *Neumann and Forsyth,* 1993] is the basis for our south MAR (SMAR) model. Gravity studies by *Kuo and Forsyth* [1988] and *Neumann and Forsyth* [1993] show a bull's-eye-shaped mantle Bouguer gravity low centered at the segment midpoint where an axial rift valley is absent. Ocean bottom seismic experiments [*Tolstoy et al.*, 1993] confirmed thinned crust at segment distal ends. We take L = 100 km, $\bar{t}_c$ = 5.5 km, and Δt_c = 2.5 km (Figure 2c).

Our fast-spreading East Pacific Rise (EPR) model is based on the segment bounded by the Clipperton and Siqueiros transforms [*Macdonald et al.*, 1988; *Madsen et al.*, 1990; *Wang and Cochran*, 1993]. Variation in crustal thickness is taken to be sinusoidal with L = 160 km, $\bar{t}_c$ = 5.5 km, and Δt_c = 0.5 km (Figure 2d).

Finally, ridge-hotspot interaction is considered in the slow spreading Reykjanes Ridge (RR) model [*Searle and Laughton*, 1981; *Bell and Buck*, 1992; *Appelgate and Shor,* 1994]. We model five short segments, each of L = 20 km, $\bar{t}_c$ = 12 km [*White et al.*, 1992], and Δt_c = 0 km. This crustal thickness model represents short segments observed along the northern Reykjanes Ridge [*Appelgate and Shor,* 1994] (Figure 2e).

Lithospheric Temperature and Rheology

In this section, we develop a 3-D steady state thermal and rheological model for a crustal layer overlying a passively upwelling mantle half-space. We focus on the thermal and rheological effects of spreading rate and along-axis variation in crustal thickness.

Three-Dimensional Thermal Balance

We use the spectral flow solution and finite difference technique of *Phipps Morgan and Forsyth* [1988] to calculate the 3-D conduction and advection of heat in a passively upwelling flow that is driven by constant-thickness plates diverging at a half-spreading rate u. Finite difference grids are densest in the upper 15 km vertically and within 20 km of the ridge axis horizontally to resolve the details of lithospheric temperature structure near the ridge axis (Figure 2).

The thermal model has been expanded to include hydrothermal cooling and the heat of magma emplacement at

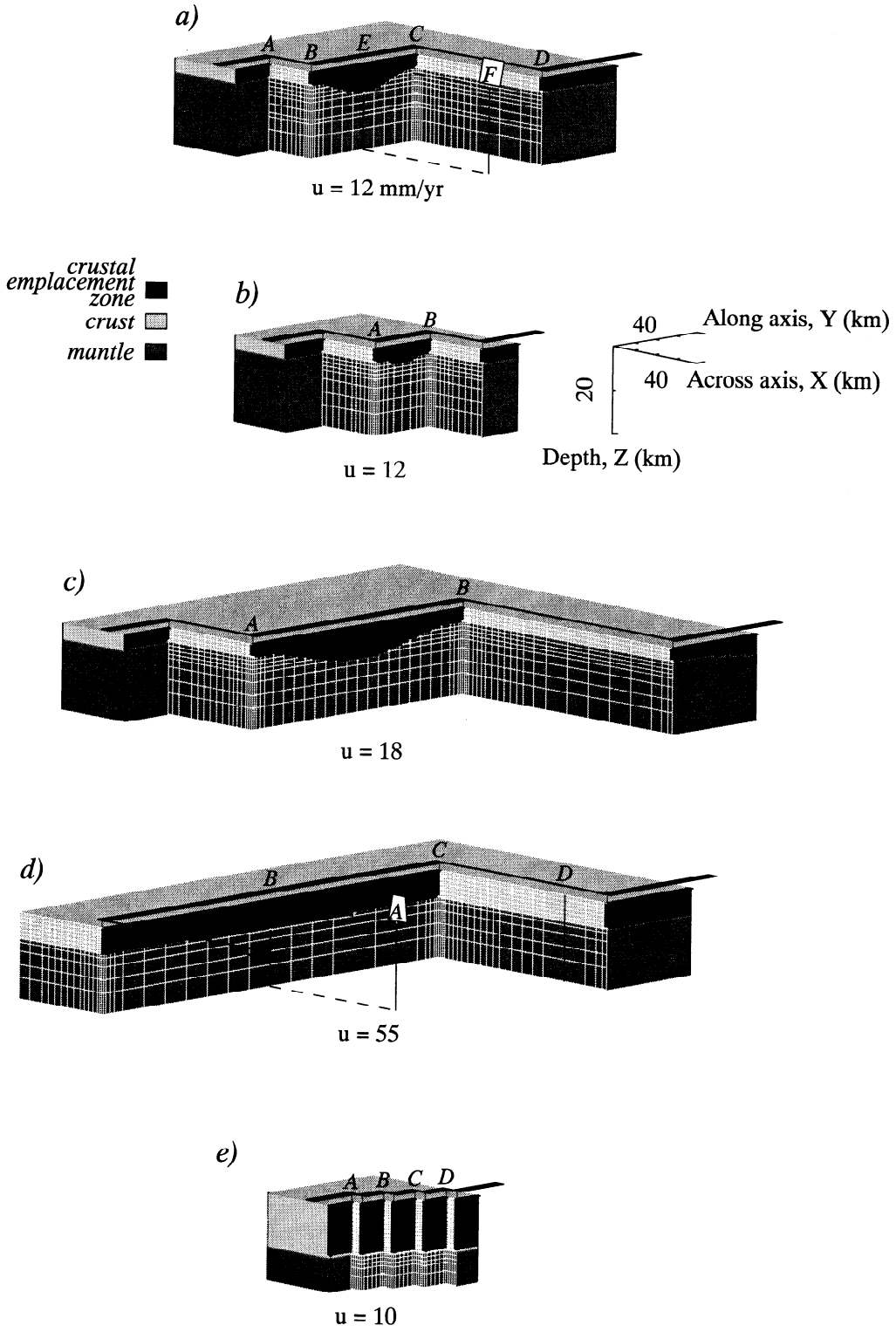

Figure 2. Segment geometry and crustal thickness inputs for various ridge models: (a) north Mid-Atlantic Ridge long segment (NMARL), (b) north Mid-Atlantic Ridge short segment (NMARS), (c) south Mid-Atlantic Ridge (SMAR), (d) East Pacific Rise (EPR), and (e) Reykjanes Ridge (RR). Thick solid lines mark ridge segments, and thin solid lines indicate offsets. Dark zones represent regions of axial crustal emplacement, and white lines show finite difference grids; u is half-spreading rate. Capital letters mark cross sections shown in subsequent figures. Vertical exaggeration is 2.

the ridge axis, both of which are important in determining the lithospheric temperature structure. The heat of magma emplacement plays a vital role in the near-surface energy balance and formation of lower crustal weak zones as envisioned by *Chen and Morgan* [1990a]. *Lin and Parmentier* [1989] demonstrated that hydrothermal cooling can buffer magma emplacement, thus explaining deep foci earthquakes at ridge crests [*Toomey et al.*, 1985, 1988]. *Lin and Parmentier*

[1989] also showed that surface heat flow calculated with a Nusselt Number *Nu* value of about 6-8 matches observations at slow spreading ridges better than a model without hydrothermal cooling.

Magma emplacement is modeled by including a heat source term at grid points within the crustal emplacement zone along the ridge axis to represent the injection temperature and latent heat of crystallizing magma. The heat source term satisfies [*Sleep*, 1975; *Neumann and Forsyth,* 1993; *Phipps Morgan and Chen,* 1993]

$$HS = \begin{cases} u(T_i + l_h/c_p)/w, & -w/2 \le x \le w/2,\ z \le t_c(y) \\ 0, \text{elsewhere.} \end{cases} \quad (1)$$

Values for magma injection temperature T_i, latent heat of magma l_h, specific heat of magma c_p, and width of emplacement zone w are listed in Table 1. Hydrothermal cooling is represented by increasing the thermal conductivity at grid points above 6-km depth and cooler than 400°C by a factor equal to *Nu* [*Phipps Morgan et al.*, 1987]. The rationale for this parameterization is that open cracks necessary for hydrothermal circulation are unlikely to form at pressure greater than that found at 6 km or temperatures greater than 400°C.

Using velocities **u** from the spectral flow solution, a finite upwind differencing method is used to solve the equation of steady state energy conservation,

Table 1. Model Parameters

Parameter	Definition	Value	Units
u	half-spreading rate	variable	mm/yr
$\bar{t}_c$	mean crustal thickness	variable	km
Δt_c	crustal thickness variation	variable	km
L	ridge segment length	variable	km
T_i	magma injection temperature	1150	°C
l_h	latent heat of magma	$7.5\text{x}10^5$	J kg^{-1}
c_p	specific heat of magma	1250	J kg^{-1} °C^{-1}
w	width of emplacement zone	1	km
κ	thermal diffusivity	10^{-6}	m^2 s^{-1}
T_m	mantle temperature	1320	°C
$\dot{\varepsilon}$	extensional strain rate	10^{-14}	s^{-1}
n_c, n_m	power of viscosity law for crust, mantle	3.4, 3	
q_c, q_m	activation energy for crust, mantle	$2.6\text{x}10^5$, $5.2\text{x}10^5$	J mol^{-1}
A_c, A_m	viscosity law constant for crust, mantle	10^2, 10^3	MPa$^{-[n_c,n_m]}$s^{-1}
θ	angle of failure (fault dip)	45	degrees
λ	pore fluid pressure ratio	0.34	
μ	coefficient of friction	0.6	
c	cohesion	$2\text{x}10^7$	Pa
ρ_w	density of water	1000	kg m^{-3}
ρ_c, ρ_m	density of crust, mantle	2900, 3300	kg m^{-3}
g	gravitational acceleration	9.8	m s^{-2}
E	Young's modulus	$7\text{x}10^{10}$	Pa
ν	Poisson's ratio	0.25	
f	fraction of extension by faulting	0.1	
γ	ratio of fault height to fault length	$1\text{x}10^{-2}$	
A_H	cross-sectional area of axial high	5	km^2
A_R	cross-sectional area of axial rift valley	variable	km^2

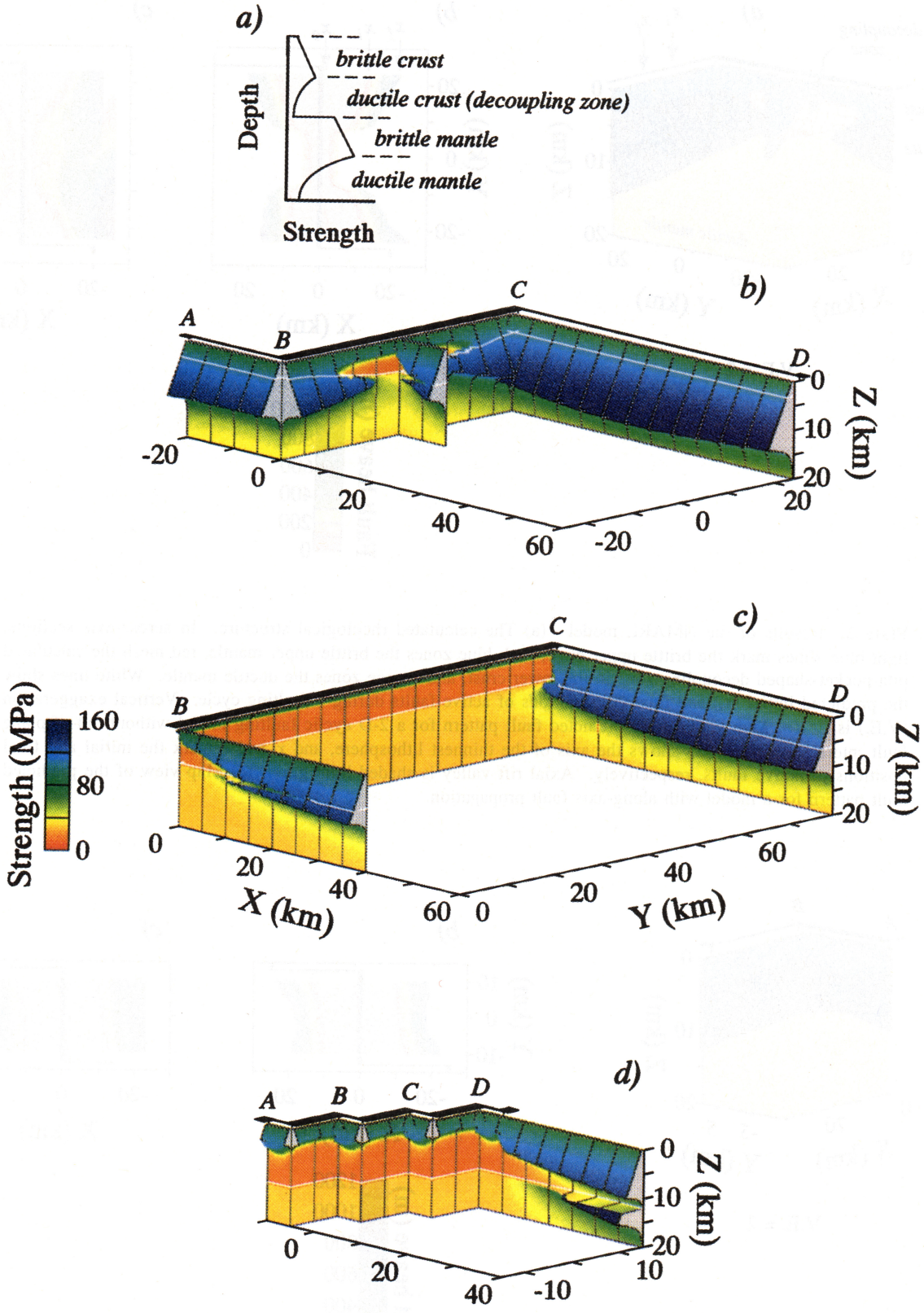

Plate 1. (a) Schematic strength envelope illustrating rheological regimes discussed in the text. Calculated strength envelope profiles are shown for (b) the NMARL, (c) EPR and, (d) RR models. Values of maximum sustainable differential strength are plotted orthogonally to the section and are color shaded. Lower crustal weak zones appear as red.

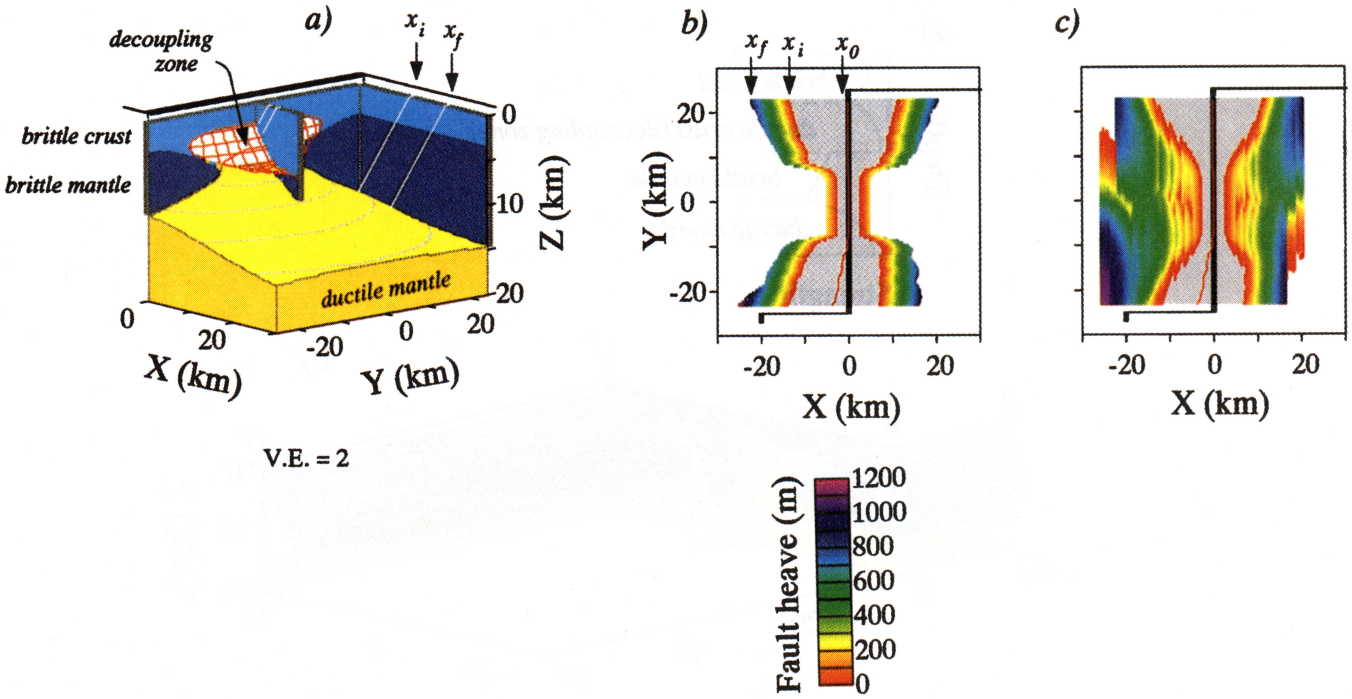

Plate 2. Results of the NMARL model. (a) The calculated rheological structure. In across-axis sections, light blue zones mark the brittle upper crust, dark blue zones the brittle upper mantle, red mesh the calculated pita-pocket-shaped decoupling zone in the lower crust, and orange zones the ductile mantle. White lines show the predicted initial (x_i) and final (x_f) positions of active faults during a faulting cycle. Vertical exaggeration (V.E.) is 2. (b) Map view of the predicted fault pattern for a 2-D cyclic faulting model without out-of-plane fault interaction. Here, x_0 shows the axis of the thinnest lithosphere, and x_i and x_f mark the initial and final positions of active faults, respectively. Axial rift valley is shaded light gray. (c) Map view of the predicted fault pattern for a model with along-axis fault propagation.

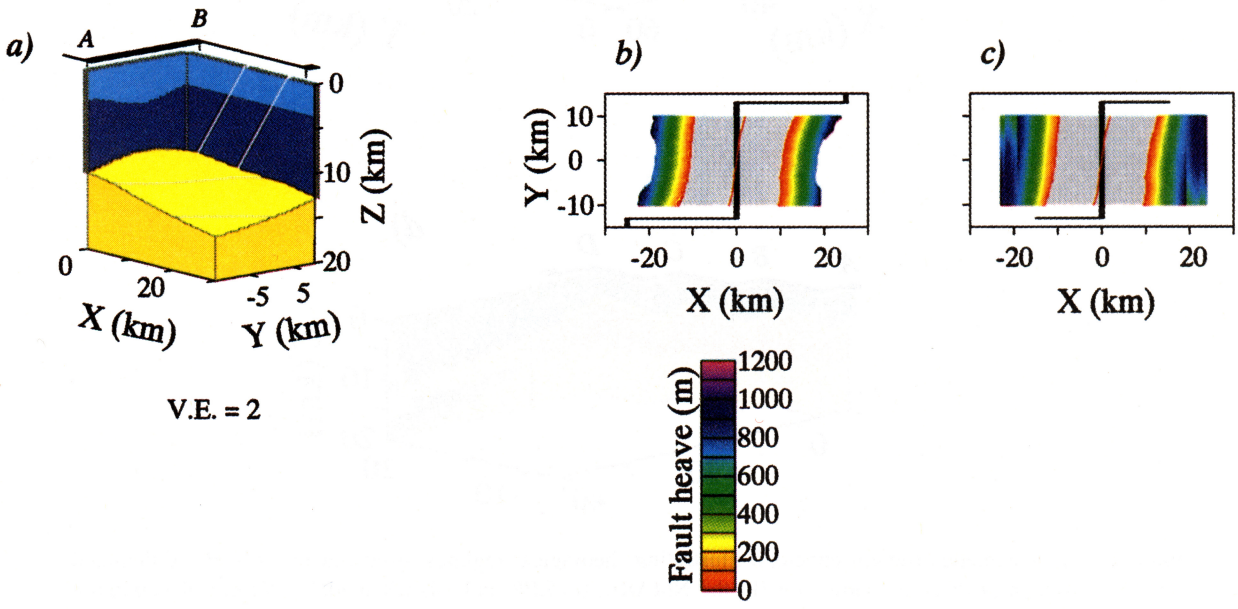

Plate 3. Results of the NMARS model. (a) The calculated rheological structure. (b) Map view of the predicted fault pattern for a 2-D cyclic faulting model without out-of-plane fault interaction. (c) Map view of the predicted fault pattern for a model with along-axis fault propagation. See Plate 2 caption for legend explanation.

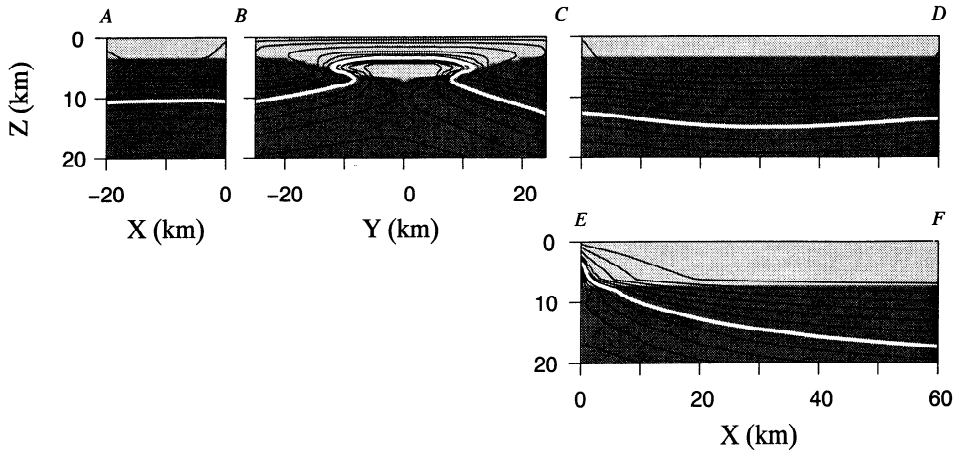

Figure 3. Calculated temperature profiles of the NMARL model with $Nu = 8$ and $\Delta t_c = 2$ km. Crust is shaded light gray, and mantle is shaded dark gray. Dark lines show the calculated temperature profiles at 100°C contour intervals. Bold white line indicates 700°C isotherm.

$$\nabla\cdot\left[\kappa Nu(z,T)\nabla T\right]+\mathrm{HS}=\mathbf{u}\cdot\nabla\mathrm{T}. \tag{2}$$

Boundary conditions include no conductive heat flow through the lateral sides of the model box; $T = 0$°C on the top boundary ($z = 0$ km); and $T = T_m$ on the bottom boundary ($z = 100$ km). Values for thermal diffusivity κ and mantle temperature T_m are listed in Table 1. We simulate ridge-hotspot interaction in the RR case by adding a temperature anomaly T_a at the bottom boundary [*Ito and Lin*, 1995a] and including a thickened crust to represent increased melt production.

Calculated temperature sections across and along the ridge axis of the NMARL model for $Nu = 8$ are shown in Figure 3. Both the effects of hydrothermal cooling, which is most effective at segment ends, and crustal thickness variations are necessary to produce significant along-axis temperature gradients. Figure 4 illustrates the temperature structure calculated for the EPR model also for $Nu = 8$. Due to small crustal thickness changes, there is little along-axis variation in temperature structure.

Crustal and Mantle Rheology

We characterize the rheology of the crust and mantle as either brittle or ductile based on Mohr-Coulomb failure criteria and a nonlinear viscosity law, respectively (see Plate 1a). The maximum sustainable differential stresses (i.e., "strength envelopes") are found by taking the minimum of a ductile flow stress and a brittle failure stress at points interpolated from the finite difference grids. The stress required to maintain ductile flow is calculated from an experimentally determined constitutive law for creep deformation

$$\dot{e} = A\left(\sigma_1-\sigma_3\right)^n \exp\left(-Q/RT\right), \tag{3}$$

where $\dot{e}$ is extensional strain rate, $\sigma_1-\sigma_3$ the differential stress, R the gas constant, and T absolute temperature [*Brace and Kohlstedt*, 1980; *Kirby*, 1983]. Following *Chen and Morgan* [1990b], we assume the entire crust behaves as diabase and the entire mantle behaves as olivine, which has stronger material properties than diabase. Values of material properties used [*Goetze*, 1978; *Shelton and Tullis*, 1981; *Kirby*, 1983; *Chen and Morgan*, 1990b] are listed in Table 1. The activation energy of the mantle was adjusted so that the predicted thickness of the brittle plate at slow spreading ridge cases matched the observed depth of seismicity [e.g., *Huang et al.*, 1986].

Taking the maximum principle stress as lithostatic overburden, sustainable brittle stresses are calculated from Mohr-Coulomb criteria using

$$\left(\sigma_1-\sigma_3\right)=\frac{(1-\lambda)\mu\rho gz+c}{\mu\sin^2\theta+\sin\theta\cos\theta}. \tag{4}$$

We choose an angle of failure θ of 45°, consistent with focal mechanism solutions of MOR earthquakes [e.g., *Huang et al.*, 1986; *Bergman and Solomon*, 1990; *Thatcher and Hill*, 1995]. Values for the pore fluid pressure ratio λ, the coefficient of friction μ, density ρ, gravity g, and cohesion c are listed in Table 1.

Decoupling Zone in the Lower Crust

Since the crust is rheologically weaker than the mantle in our models, a ductile decoupling zone may form in the lower crust [*Chen and Morgan*, 1990a] that separates brittle crust from strong upper mantle (Plate 1a). The top of such a decoupling zone is defined thermally with its shape controlled by spreading rate and hydrothermal cooling. The base of a

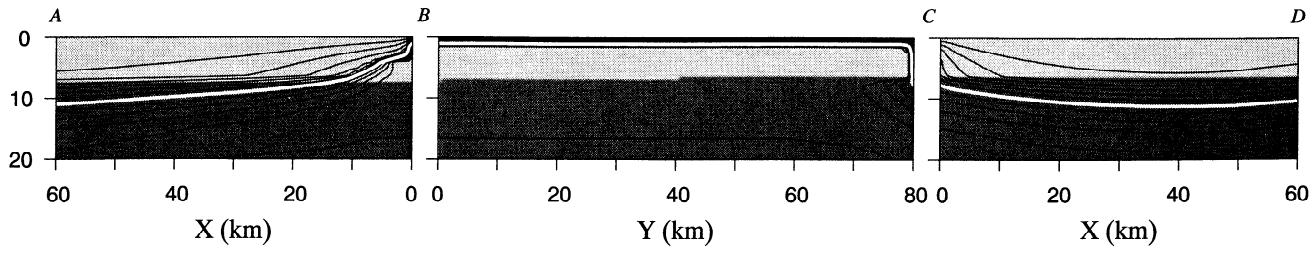

Figure 4. Calculated temperature profiles for the EPR model with $Nu = 8$ and $\Delta t_c = 0.5$ km. See Figure 3 caption for legend explanations.

decoupling zone follows the bottom of the crust, which varies along axis. Where significant crustal thinning occurs toward segment ends, as in the NMARL case, the decoupling zone wanes accordingly and may even disappear, leaving the crust and mantle in welded brittle contact at segment distal ends (Plate 1b). We dub the resulting rheological structure a "pita-pocket" feature. The temperature profiles in Figure 3 show that both along-axis crustal thickness variations and hydrothermal cooling are required for this type of structure to exist. In contrast, the along-axis uniformity of the EPR temperature creates a continuous decoupling zone (Plate 1c). In the RR case, deep emplacement of crust forms a voluminous decoupling zone with intersegment continuity (Plate 1d).

Another predicted rheological difference among various ridge models is the nature of brittle mantle continuity across the ridge axis. In the NMARL case, the brittle mantle is welded across-axis except in the centermost portion (Plate 1b). However, in the EPR case, the brittle mantle is discontinuous across-axis except within 5 km of an offset (Plate 1c). The brittle mantle in the RR case (Plate 1d) is discontinuous along the entire length of the ridge axis. These rheological differences are important in controlling the style of lithospheric deformation, because if the brittle mantle is discontinuous across axis, lithospheric extension at mantle depths can be accommodated entirely by ductile mantle flows rather than brittle faulting. Details of the predicted shape of lower crustal decoupling zones and continuity of brittle upper mantle are illustrated in Plates 2a-6a and Figure 7a.

Lithospheric Deformation

Our investigation of MOR deformation focuses on lithospheric extension of 2-D depth sections across the ridge axis. The underlying principle of the model is that active faulting occurs on planes that minimize the resistance to cohesive, frictional, and plate flexural forces. The model is cyclical in that only one fault is active at a time on either side of the ridge axis. We assume faults initiate near the ridge axis where the lithosphere is weakest. The fault grows and is moved off-axis by dike injection until it becomes more favorable to initiate a new fault near the axis.

Across-Axis Force Balance

We apply the flexural model of extensional faulting of *Forsyth* [1992], considered in the context of MOR deformation by *Shaw and Lin* [1993], to across-axis sections. The model is based on a thin-plate approximation to constant-thickness elastic lithosphere overlying an inviscid asthenosphere. When subjected to an applied horizontal regional stress $\sigma_1 - \sigma_3$ in the direction of spreading, the lithosphere is assumed to fail along planar normal faults which cut its entire thickness. To initiate a new fault, the applied stress must equal the sum of cohesional σ_c and frictional σ_f stresses on the fault plane. During a faulting cycle, extension continues along the broken fault (which no longer has any cohesional strength) as it moves away from the ridge axis until a final state of stress exceeds the initial state, $(\sigma_f + \sigma_e)_{\text{final}} > (\sigma_f + \sigma_c)_{\text{initial}}$, where σ_e is the elastic stress induced by plate flexure to accommodate finite amplitude fault displacement [*Forsyth*, 1992]:

$$\sigma_c = \frac{c}{\mu \sin^2\theta + \sin\theta\cos\theta}, \tag{5}$$

$$\sigma_f = \frac{(1-\lambda)\mu\rho g}{\mu \sin^2\theta + \sin\theta\cos\theta}, \quad \text{and} \tag{6}$$

$$\sigma_e = \tan^2\theta \left\{ E\left[(\rho_m - \rho_w)g\right]^3 / 3\left(1-\nu^2\right) \right\}^{1/4} \Delta x H^{1/4}. \tag{7}$$

Values of Young's modulus E, Poisson's ratio ν, and the densities of mantle ρ_m and seawater ρ_w are listed in Table 1. Neglecting rotation of fault planes, the above stress terms depend only on lithospheric thickness H and fault heave Δx. At the end of a faulting cycle, the active fault reaches a maximum heave $\Delta x_{\max}$ and a corresponding maximum height $h_{\max} = \Delta x_{\max} \tan(\theta)$. The predicted fault spacing is $s = h_{\max}/f$, where f is the percentage of seafloor spreading by lithospheric stretching. We take $f = 0.1$ for all cases, which is at the lower end of the estimated range of 0.05-0.2 for slow spreading ridges [e.g., *Solomon et al.*, 1988; *Shaw and Lin*, 1993]. Our force balance calculations consider the effect of thickening lithosphere.

We classify lithospheric sections into three categories based on their primary rheological characters (Figure 5). "Intact" structure, the strongest, is characterized by the lack of a decoupling zone and by a brittle mantle that is welded across axis. "Cavity" structure has a decoupling zone underlain by welded brittle mantle. "Notched" structure, the weakest, contains a lower crustal weak zone and discontinuous brittle mantle across axis.

Using the criteria of minimum resistance forces for fault motion, we obtain a steady state solution of cyclic faulting. We argue that faults are most likely to initiate near-axis and thus place the bottom of the initial fault plane at the lithosphere's thinnest point at $x = x_0$. The along-axis position of x_0 is hereafter referred to as fault axis. The surficial expression of this initial fault plane is at $x_i = x_0 \pm H_i \tan(\theta)$, and the conjugate initial fault planes on each sides of the ridge axis define an axial rift valley of width $2H_i \tan(\theta)$, (see Figure 5). Faults forming in an "intact" structure must break the entire lithosphere for extension to occur (Figure 5b). Faults in a "notched" structure, however, need only break the brittle crust, since the underlying mantle can deform in a ductile manner (Figure 5d). Faulting behavior in a "cavity" structure may be more complex; for simplicity, we assume that a "cavity" structure produces faults in a similar manner as an "intact" structure, neglecting any effects an isolated decoupling zone may have in fault formation. In reality, two scales of faulting may form near the axis with wavelengths controlled by the thicknesses of the decoupled brittle crust and mantle, respectively.

We next iteratively calculate the forces required to continue motion on an existing fault plane as it is rafted off axis. Depending on initial lithospheric thickness and off-axis thickening rate, a fault will stop growth at $x = x_f$ when the forces required for further motion on an old fault plane become greater than those required to break a new one. At this point, a new fault is expected to form near the ridge axis at x_i, completing a faulting cycle. Therefore, x_f-x_i is the surficial expression of the active fault zone and hence also the predicted fault spacing s (Figure 5a). Performing this calculation on a series of across-axis sections results in maps of predicted along-axis faulting style (Plates 2b-6b and Figure 7b).

Along-Axis Fault Propagation

The 2-D cross-sectional model presented above neglects the possibility of along-axis growth of individual faults and their

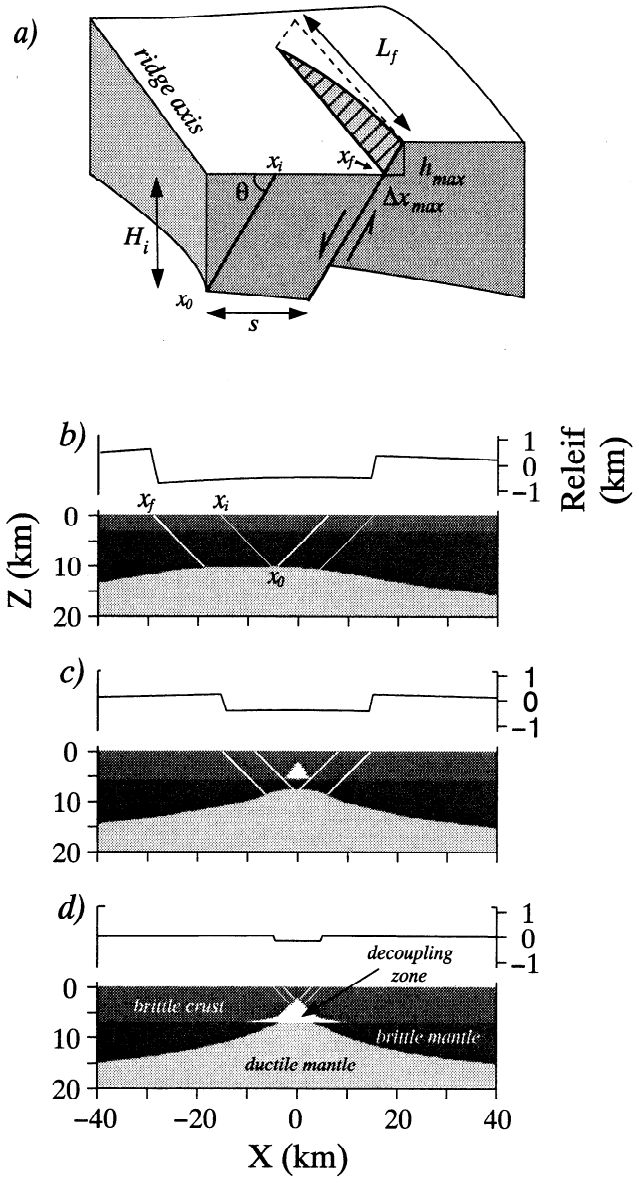

Figure 5. (a) Schematic diagram illustrating the concept of a cyclic faulting model. H_i is lithospheric thickness at the ridge axis, θ is fault dip angle, and L_f is along axis fault length. Each active fault initiates at distance x_i from the ridge axis at the beginning of a faulting cycle and reaches its maximum height (h_{max}) and heave (Δx_{max}) by the end of the cycle, when the fault has traversed to a final location $x_f = x_i + s$. Outboard of the active fault, dormant faults are predicted at a regular spacing of s. Using the results of the NMARL model as an example, ridge-axis rheological structures are classified into three categories: (b) intact, where lower crustal decoupling zone does not exist and brittle mantle is welded across the ridge axis; (c) cavity, where an isolated decoupling zone exists but the brittle mantle is still welded across the ridge axis; and (d) notched, where a decoupling zone exists and the brittle mantle is discontinuous beneath the ridge axis. Cross sections in (b)-(d) represent a progression from segment distal ends to the segment center.

interaction. In this section, we formulate a model of along-axis fault propagation and apply it to two end-member cases of fault interaction. Using the Dugdale-Barenblatt model of crack growth, *Cowie and Scholz* [1992a] argue that the maximum displacement on a fault is limited by its along-strike length. Based on most continental and some oceanic crustal examples, *Cowie and Scholz* [1992b] and *Dawers et al.* [1993] found an approximate linear relationship between the maximum fault displacement d and the along-strike length L_f,

$$d = \gamma L_f, \tag{8}$$

where the constant γ is approximately $5-9\times10^{-3}$ in a MOR setting [*Cowie et al.*, 1993; *Carbotte and Macdonald*, 1994b]. This can be translated into the dependence of fault length on fault heave Δx and dip angle θ as $L_f = \Delta x/\gamma\sin(\theta)$. In the following calculations, we take $\gamma = 10^{-2}$.

The Dugdale model assumes plane strain, which is why the lithospheric thickness H was not considered in the scaling law of *Cowie and Scholz* [1992a]. This scaling law is thus not strictly valid in regions of variable lithospheric thickness. We attempt to incorporate an H dependence by requiring that as faults incrementally grow from an original length L_f^1 to a new length $L_f^2 = L_f^1 + dL_f^{thin} + dL_f^{thick}$, the newly ruptured fault plane areas on both ends should be equal:

$$dL_f^{\text{thin}} H^{\text{thin}} = dL_f^{\text{thick}} H^{\text{thick}}, \tag{9}$$

where H^{thin} and H^{thick} are plate thicknesses at the thinner and thicker ends of the fault plane, respectively, and dL_f^{thin} and dL_f^{thick} are corresponding growth increments (Figure 6a). This stipulation requires elastic strain energy to be released evenly at either end of the fault during a rupture event. Along the fault length, the displacement is given by a tapered profile predicted by the Dugdale model [*Cowie and Scholz*, 1992a].

Within this framework, we consider two end-member cases of fault interaction. In the first end-member case, faulting is confined within 2-D across-axis sections, and there is no interaction between out-of-plane faults (Plates 2b-6b). In the second end-member case, in contrast, the active fault in each across-axis section was allowed to grow along axis according to the scaling laws of individual faults (Figure 6b). For an individual across-axis section, $y = y_i$, the fault height, $h_i(x,y)$, achieved during one faulting cycle was predicted for every location in the whole region. Such calculations were carried out for all across-sections y_i. Finally, for each point in the region (x_0, y_0), a characteristic value of fault height was obtained by retaining the maximum $h_i(x_0, y_0)$ (Plates 2c-6c). The dynamical effects of along-axis fault growth were not considered. A thorough understanding of fault interaction requires a fully 3-D analysis that is the subject of future investigation. Applications of these end-member scenarios to various ridge models are shown in next section.

Model Results

In this section, we discuss in detail the predicted fault patterns in various ridge models and use these results to interpret the observed MOR faulting style in terms of subseafloor thermal and rheological structure. For each model in Plates 2-6, we present a 3-D diagram of the calculated rheological structure and map views of the predicted fault patterns without out-of-plane fault interaction and with along-axis fault propagation.

Slow Spreading Ridges

The pita-pocket-shaped decoupling zone is evident in the NMARL model (Plate 2a). Drastic differences in the predicted fault patterns are seen between the "intact" and "notched" cross-sections of Plate 2a. Faults initiate farther off axis, and

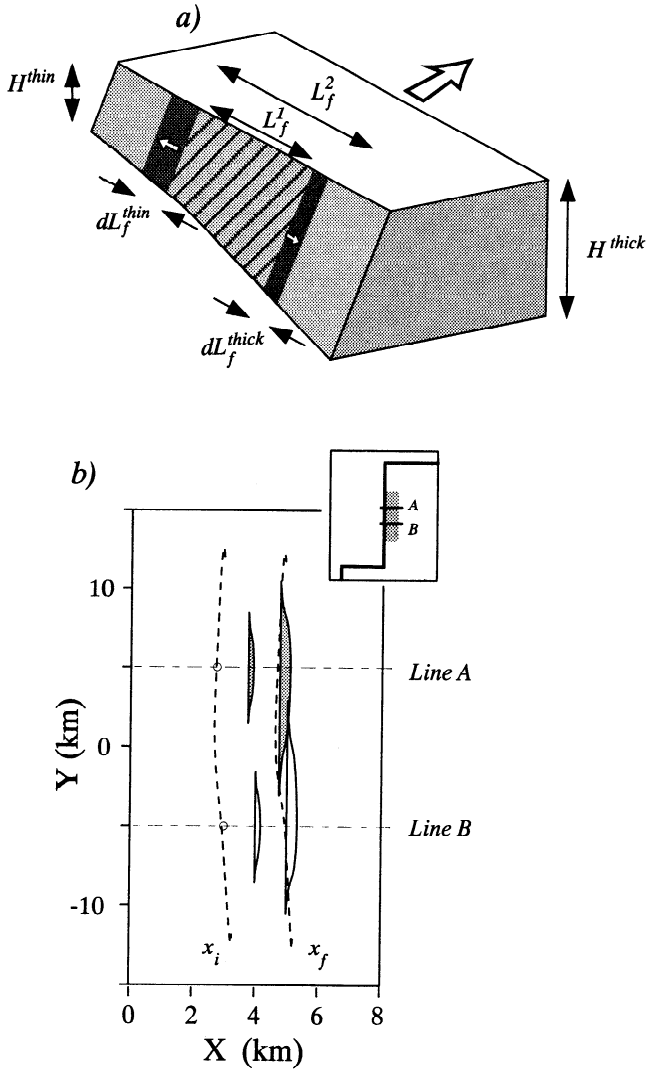

Figure 6. (a) Schematic diagram showing along-axis fault propagation in a variable thickness plate. The fault plane is assumed to grow along axis by rupturing equal areas at the two fault ends. (b) Map view of the calculated displacement-length profiles for two across-axis lines (lines A and B) in the NMARL model. Here, x_i and x_f are the predicted initial and final positions of the fault plane, respectively. As a fault is rafted away from x_i to x_f, its maximum displacement and along-axis length increase. Note that faults are predicted to grow preferentially toward the segment center ($Y = 0$ km), where the lithosphere is the thinnest.

the resultant axial valleys are wider, in the intact structure than the notched structure (Plate 2b). Faults at segment ends also accommodate more displacements, resulting in larger fault height and spacing than at the segment center. Plate 2c shows that along-axis fault propagation may significantly affect fault patterns. Large faults that formed at segment ends are predicted to propagate as much as 30 km into the segment center. The along-axis variability in the predicted fault patterns (Plates 2b and 2c) is comparable to the observed faulting style at the MAR near 29°N, where small (200-400 m) and narrowly spaced (1-3 km) faults occur near the segment center, while large (~1 km) and widely spaced (6-9 km) faults occur near segment ends [*Shaw*, 1992; *Shaw and Lin*, 1993].

A combination of thin crust and short ridge segments in the NMARS model results in a cold, strong lithosphere, forming an intact structure along the entire segment length (Plate 3a). Large faults are predicted to be a dominant axial feature (Plates 3b and 3c). Ridge segments adjoining short offsets are predicted to influence each other thermally, causing the fault axis to curve toward adjacent segments and producing large faults at inside-corner crust. These predicted fault patterns resemble well the pronounced axial rift valley and curved faults along a short MAR segment near 28°50'N [*Sempéré et al.*, 1993].

The SMAR model (Plate 4) predicts dramatic along-axis changes in the rheological structure (Plate 4a) and fault patterns (Plates 4b and 4c) at this slow spreading segment. Because the SMAR segment is 100 km long, large faults at segment distal ends are unable to propagate into the segment center, leaving the middle portion of the segment with only small faults and a narrow axial rift valley (Plate 4c). This prediction resembles remarkably well the axial morphology of the long MAR segment near 34°S, where the axial rift valley disappears at the centermost portion of the ridge segment [*Kuo and Forsyth*, 1988; *Grindlay et al.*, 1991; *Neumann and Forsyth*, 1993].

Fast Spreading Ridges

Due to the dominance of notched structure in the EPR model (Plate 5a), fast spreading ridge segments are predicted to have much smaller variations in fault height (100-200 m) and spacing (1-2 km) (Plates 5b and 5c). Faults with predicted heights greater than 100-200 m are limited to within a few kilometers of an offset, in general agreement with the observed axial morphology of the EPR near 10°N [e.g., *Carbotte and Macdonald*, 1994a,b]. However, observations suggest that large normal faults could still form 20-30 km from the axis at fast spreading ridges [*Lee and Solomon*, 1995]. This may be due to the fact that lithosphere at fast spreading ridges thickens more gradually away from the ridge axis and thus the tendency for concentrated deformation at the ridge axis is less profound.

Hotspot-Affected Ridges

The anomalously thick crust of the RR model creates a voluminous lower crustal decoupling zone (Plate 6a). The excess heat released by the solidification of this thick crust causes an anomalously hot upper mantle. Consequently, the lithosphere is predicted to have a notched structure along the entire ridge length. The predicted brittle upper crust is, however, thicker than in the EPR case, resulting in slightly wider axial rift valleys (Plates 6b and 6c). The predicted fault height and spacing are much smaller than other sections of the MAR, but greater than those of the EPR. The overall trend of the calculated active fault zone follows the regional direction of the ridge axis but is oblique to each individual segment (Plates 6b and 6c). Such a predicted fault pattern resembles the oblique fault trends observed at the Reykjanes Ridge [*Searle and Laughton*, 1981; *Appelgate and Shor*, 1994].

Discussion

The 3-D temperature rheological models and 2-D cyclic faulting concept presented above are significant improvements over previous 2-D continuum deformation models [e.g., *Phipps Morgan et al.*, 1987; *Lin and Parmentier*,

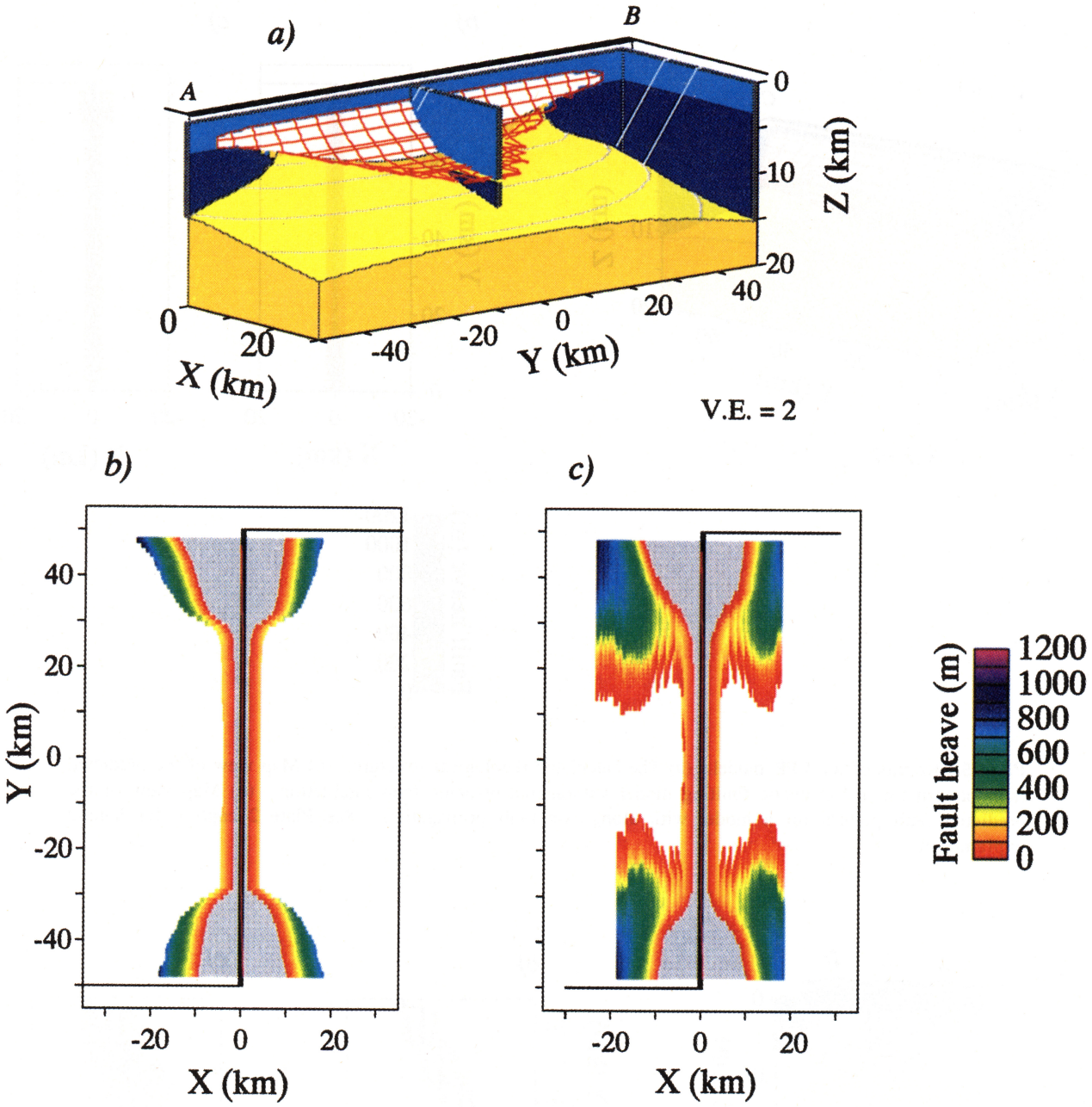

Plate 4. Results of the SMAR model. (a) The calculated rheological structure. (b) Map view of the predicted fault pattern for a 2-D cyclic faulting model without out-of-plane fault interaction. (c) Map view of the predicted fault pattern for a model with along-axis fault propagation. See Plate 2 caption for legend explanation.

1989; *Chen and Morgan,* 1990a,b; *Phipps Morgan and Chen,* 1993] in two aspects: (1) the new 3-D temperature models consider explicitly the important effects of along-axis variation in crustal thickness; and (2) the new cyclic faulting model predicts detailed morphology of discrete faults rather than just a gross topography. These new models extend our ability to interpret fine-scale ridge crest morphology in terms of subseafloor temperature and rheological structure. The following sections discuss the implications for the models to two most prominent seafloor features, abyssal hill morphology and axial rift valley.

Abyssal Hill Morphology

Abyssal hills on ocean basins are thought to form by a combination of volcanic and tectonic processes [e.g., *Searle and Laughton*, 1977; *Goff*, 1991; *Malinverno*, 1991; *Goff et al.,* 1995]. Studies by *Bergman and Solomon* [1990] and *Shaw and Lin* [1993], however, support the hypothesis that abyssal hills at slow spreading crust are primarily expressions of rotated normal fault blocks. We use combined statistical data on the heave and spacing of individual faults and abyssal hills to test the predicted fault patterns from various ridge models.

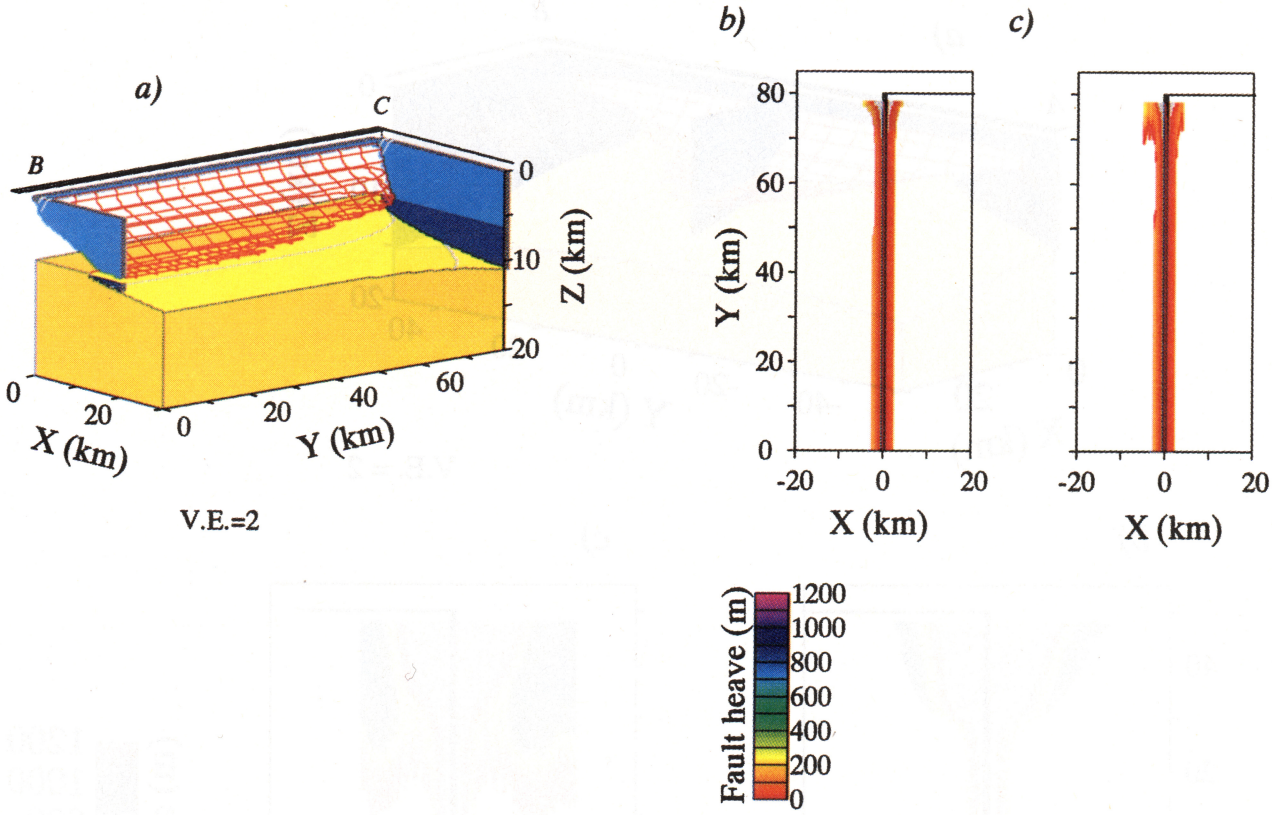

Plate 5. Results of the EPR model. (a) The calculated rheological structure. (b) Map view of the predicted fault pattern for a 2-D cyclic faulting model without out-of-plane fault interaction. (c) Map view of the predicted fault pattern for a model with along-axis fault propagation. See Plate 2 caption for legend explanation.

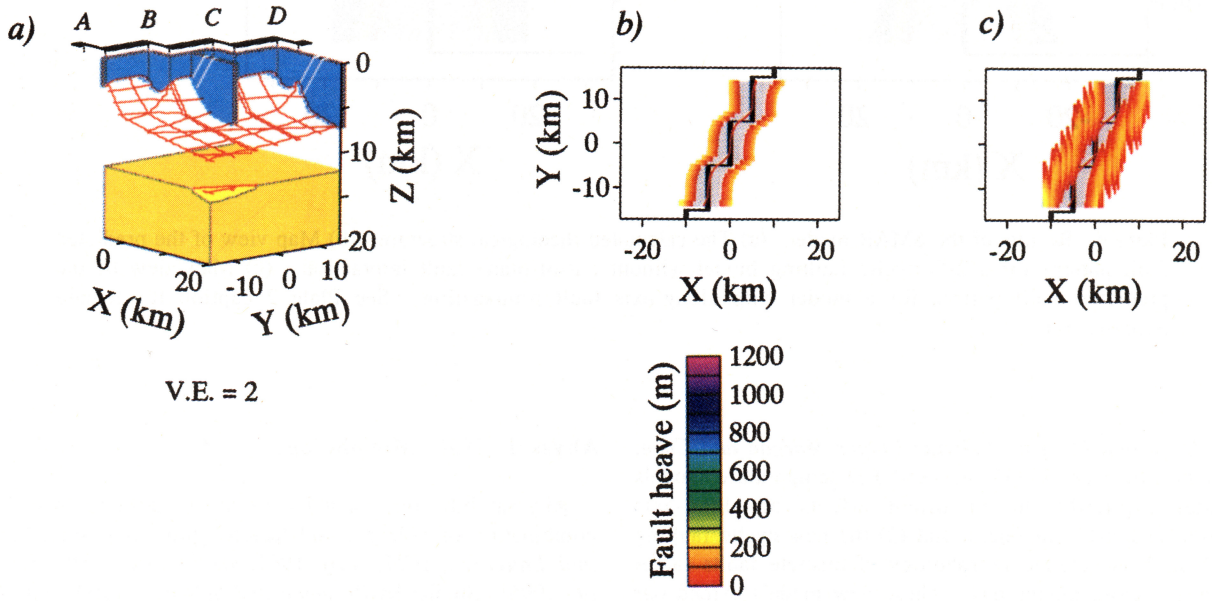

Plate 6. Results of the RR model. (a) The calculated rheological structure. (b) Map view of the predicted fault pattern for a 2-D cyclic faulting model without out-of-plane fault interaction. (c) Map view of the predicted fault pattern for a model with along-axis fault propagation. See Plate 2 caption for legend explanation.

We first compare the results of the NMARL model with the observed variations in abyssal hill characteristics on the western flank of the MAR near 25°25'-27°10'N [*Goff et al.*, 1995] (Figure 7). Values of crustal thickness in the region are derived from the residual gravity analysis of *Lin et al.* [1993]. Also shown are data on fault heave and spacing obtained at the segment center (thick crust) and distal ends (thin crust) of the MAR near 29°N [*Shaw*, 1992; *Shaw and Lin*, 1993]. The predicted values of fault heave (Figure 7a) and spacing (Figure 7b) decrease with increasing crustal thickness, in general agreement with the observations. The predicted heaves are somewhat systematically greater than the abyssal hill data of *Goff et al.* [1995], which gave only average values over ~50-km-long profiles.

Comparisons of model predictions with global data sets as a function of spreading rate are shown in Figure 8. As examples, statistical results of the observed heave (Figure 8a) and spacing (Figure 8b) of faults and abyssal hills are shown for four data sets of *Searle and Laughton* [1977], *Goff* [1991], *Malinverno* [1991], and *Carbotte and Macdonald* [1994b]. These four statistical data sets were chosen because each encompasses a range of spreading rates, although we recognize that many of these data are only averaged values over wide areas without detailed knowledge of their specific location within a segment. These limited data sets therefore reflect only a small fraction of the full spectrum of the observed variabilities in MOR faulting style. *Shaw* [1992] and *Shaw and Lin* [1993] have observed values of fault heave (100-1000 m) and spacing (1-10 km) at a half-spreading rate of 12-14 mm/yr along the MAR near 27°30'-31°N (Figures 8a and 8b). These observed variabilities in fault heave are much greater than the rest of the averaged data sets shown in Figure 8a. To first order, the various ridge models predict successfully decreases in fault heave and spacing with increasing spreading rate (Figures 8a and 8b).

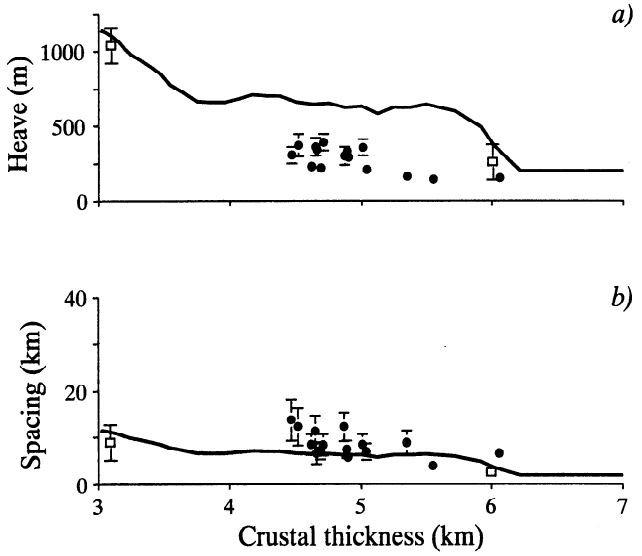

Figure 7. The predicted (a) fault heave and (b) spacing as a function of crustal thickness based on the NMARL model (solid lines). Solid dots show abyssal hill morphology [*Goff et al.*, 1995] versus crustal thickness [*Lin et al.*, 1993] from data collected on the western flank of the MAR near 25°25'-27°10'N. Solid squares show data on fault heave and spacing obtained at the segment center (thick crust) and distal ends (thin crust) of the MAR near 29°N [*Shaw*, 1992; *Shaw and Lin*, 1993]. Error bars for data points are also shown.

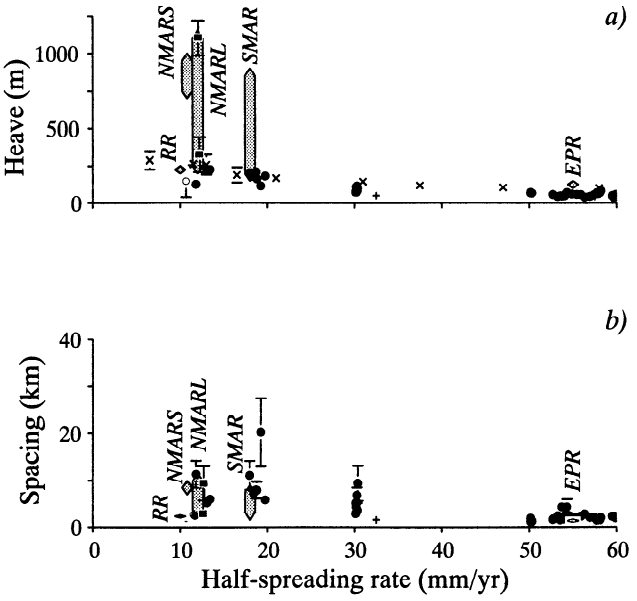

Figure 8. The predicted ranges of (a) fault heave and (b) spacing as a function of spreading rate based on the results of various ridge models (shaded bars). As examples, statistical results of the observed heave and spacing of faults and abyssal hills are shown for four data sets from *Goff* [1991] (solid dots), *Malinverno* [1991] (crosses), *Laughton and Searle* [1977] (open circles), and *Carbotte and Macdonald* [1994b] (plus signs). Errors bars for data points are also shown. Note that these limited data sets may reflect only a small fraction of the full spectrum of the observed variabilities in MOR faulting style. Solid squares show data on fault heave and spacing obtained at the MAR near 29°N [*Shaw*, 1992; *Shaw and Lin*, 1993], revealing much larger variations in fault heave (100-1000 m) than the other limited data sets.

Axial Rift Valley

The mid-ocean ridge system exhibits remarkable variability in ridge axis morphology with an axial high often observed at fast spreading ridges and an axial rift valley at slow spreading ridges [e.g., *Macdonald*, 1982]. We calculate the cross-sectional area of an axial rift valley, A_R, formed by the largest faults that occur on either side of the ridge axis. Based on the across-axis area of magma-chamber-supported isostatic topographic highs observed on the axes of fast spreading ridges [*Macdonald*, 1982; *Wang and Cochran*, 1993] and neovolcanic ridges observed on the axes of slow spreading ridges [*Smith and Cann*, 1992; *Sempéré et al.*, 1993], the cross-sectional area of magmatic axial high features, A_H, is estimated to be of the order of 5 km^2. Therefore if A_R is much smaller than A_H, an axial topographic high is expected (Figure 9a, top). In contrast, if A_R is much greater than A_H, a dominant axial rift valley is expected (Figure 9a, bottom). We have calculated axial rift valley area as a function of distance from the segment midpoint for end-member models without out-of-plane fault interaction (Figure 9b) and with along-axis fault propagation (Figure 9c).

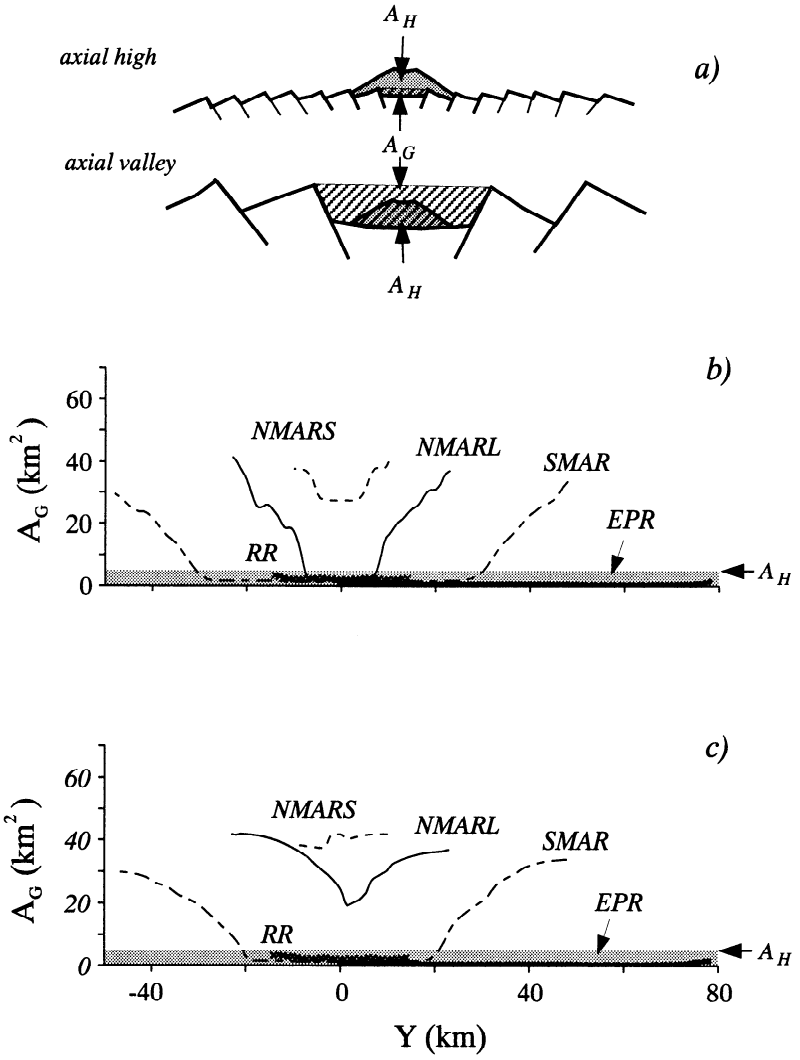

Figure 9. (a) Schematic diagram showing ridges of contrasting axial topography. If the cross-sectional area of an axial rift valley A_R is much smaller than the size of neovolcanic features A_H, a dominant axial topographic high is expected (top). In contrast, if A_R is much greater than A_H, a dominant axial rift valley is expected (bottom). (b) The calculated cross-sectional areas of axial valleys for various ridge models without out-of-plane fault interaction. Light gray bar shows an estimated cross-sectional area of neovolcanic features (A_H = 5 km^2). (c) The predicted cross-sectional areas of axial rift valleys for various ridge models with along-axis fault propagation.

Results in Figure 9 show that along-strike fault propagation is necessary to explain the along-axis continuity of the large rift valley in the NMARL model. In the SMAR case, however, large distal faults cannot traverse into the segment center even if along-axis fault propagation is considered. This supports the hypothesis that the disappearance of the rift valley at the MAR near 32°-34°S [*Kuo and Forsyth*, 1988; *Neumann and Forsyth*, 1993] is due to the anomalously thick crust at the segment center. In contrast, the axial rift valley sizes of the EPR and RR models are predicted to be smaller than neovolcanic or isostatic features, in general agreement with observations. It has been documented that the percentage of outward facing faults in the entire fault population increases from ~20% at slow spreading rates to ~50% at the fastest spreading rates [*Carbotte and Macdonald*, 1994b]. An increase in the number of outward facing faults could further decrease the predicted size of axial rift valleys at a fast spreading ridge.

Effects of Crustal Thickness and Segmentation

The above model results support the hypothesis that crustal thickness is a key variable in producing variations in faulting style. At slow spreading ridge segments, for example, a 50% reduction in crustal thickness can lead to a twofold to threefold increase in fault spacing and height (Plate 2 and Figure 8). In contrast, the uniform crustal thickness at the EPR produces uniform fault patterns (Plate 5). For hotspot-affected ridge segments, the dominant cause of a weak lithosphere is an overthickened crust rather than elevated mantle temperatures. Thus our model results suggest a cause-and-effect relation between variations in crustal thickness (Figure 1a) and fault characteristics (Figures 9b and 9c).

Offset length can also affect faulting if it is small enough to allow thermal interaction between two adjacent segments. As a result of such interaction, the fault axis may curve into the inside-corner crust (Plate 3b). This effect may also cause

larger faults at the inside-corner crust than at outside-corner crust. Together with the inherent weakness caused by transform faults, this predicted asymmetry may contribute to the formation of inside-corner topographic highs as observed at slow spreading crust [*Karson and Dick*, 1983; *Kuo et al.*, 1984; *Severinghaus and Macdonald*, 1988; *Tucholke and Lin*, 1994; *Escartìn and Lin*, 1995].

The last important geometrical factor is segment length. The segment length may have two direct effects on faulting: (1) a ridge composed of short segments loses heat more effectively than a ridge composed of long segments; and (2) since the largest faults prefer to occur at segment distal ends, their ability to reach the segment center is limited by the segment length.

Model Limitations

The purpose of this study is to address the theoretical relationships between lithospheric deformation and external tectonic variables such as crustal thickness, spreading rate, and segmentation. Limitations of model predictions result from uncertainties in model parameters and model assumptions including the following:

1. The rheological laws we used to model dislocation creep are constrained only by laboratory experiments on samples of diabase and olivine [*Goetze*, 1978; *Shelton and Tullis*, 1981; *Kirby*, 1983], which are not completely representative of the oceanic crust and mantle. Furthermore, creep is affected by the water content of rock. It is possible that the lower crust is drier than expected due to the partitioning of water into melt (*G. Hirth*, personal communication, 1995). Differences between the water content of laboratory samples and the lower crust will lead to different predicted values of lithospheric strength.

2. The thermal models we used to determine lithospheric strength rely on crustal thickness as an input. Although we have used seismic observations when possible, in most cases, only gravity measurements were available. Comparisons of seismic and gravity results obtained in a few areas in the Atlantic suggest that gravity-derived crustal thickness models may systematically underestimate the seismic crustal thickness [*Minshull et al.*, 1995; *Tolstoy et al.*, 1993]. Therefore for cases for which only gravity data are available, we may have underestimated along-axis variations in lithospheric strength and faulting style.

3. Limitations in the validity of the thermal model also include the assumption of steady state behavior and the lack of convective heat transfer in the crustal magma chamber of our thermal model. The emplacement of magma at ridges is episodic in nature so that our model applies only in a time-averaged sense. Episodic crustal accretion may lead to the cold crust observed at Iceland as indicated by heat flow and seismic measurements [*Menke and Sparks*, 1995]. By neglecting crustal mush convection, which may lead to more heat loss [*Wilson et al.*, 1988], we may have systematically underestimated the strength of the near-axis crust.

4. Our faulting models did not consider inside- versus outside-corner crustal asymmetry, which is most profound at slow spreading ridges. Crustal asymmetry near transforms may be caused by the mechanical weakness of the transform fault [*Karson and Dick*, 1983; *Kuo et al.*, 1984; *Severinghaus and Macdonald*, 1988; *Tucholke and Lin*, 1994; *Escartìn and Lin*, 1995], an effect not accounted for in this model. Our thermal model shows that thermal interaction between segments contributes to asymmetry, especially at short offsets.

Conclusions

Results of our 3-D models of temperature and rheological structure and 2-D models of cyclic faulting suggest the following theoretical relationships:

1. Crustal thickness variations and hydrothermal cooling are necessary to create significant along-axis temperature gradients. Where strong along-axis temperature and crustal thickness gradients exist, a pita-pocket-shaped decoupling zone may form at the lower crust of a slow spreading ridge segment. At fast spreading and hotspot-affected segments, a uniform decoupling zone is predicted along the whole ridge length.

2. Model results suggest a strong dependence of faulting style on crustal thickness, since its variations play an important role in controlling ridge-axis temperature and rheological structure. Slow spreading segments are predicted to have relatively large along-axis variations in fault height and spacing. In contrast, the fast spreading and hotspot-affected segments are predicted to have smaller variations in fault styles, except in the immediate vicinity of a major transform fault.

3. The presence or lack of a steady state axial rift valley is also predicted to depend on crustal thickness, spreading rate, and the ability of rift-bounding normal faults to propagate along axis. For fast spreading and hotspot-affected segments, the axial rift valleys are predicted to be small, and their sizes may not be distinguishable from those of axial topographic highs. This is in contrast to most slow spreading segments, where axial rift valleys are predicted to be a dominant morphological feature. For a slow spreading segment of great length, however, the axial rift valley size is predicted to diminish toward the segment center because large faults formed at segment distal ends cannot propagate through a large decoupling zone created by locally thickened crust at the segment center.

Acknowledgments. We benefited from discussion with B. Tucholke, J. Escartìn, G. Hirth, and A. Freed and review of the manuscript by S. Carbotte, G. Neumann, N. Sleep, G. Ito, R. Detrick, J. Escartìn, and G. Hirth. This work was supported by NSF grant OCE-9302915 and ONR grant N00014-91-J-1433. Woods Hole Oceanographic Institution contribution 9069.

References

Appelgate, B., and A. N. Shor, The northern Mid-Atlantic and Reykjanes ridges: Spreading center morphology between 55°50'N and 63°00'N, *J. Geophys. Res., 99*, 17,935-17,956, 1994.

Bell, R. E., and W. R. Buck, Crustal control of ridge segmentation inferred from observations of the Reykjanes Ridge, *Nature, 357*, 583-586, 1992.

Bergman, E. A., and S. C. Solomon, Earthquake swarms on the Mid-Atlantic Ridge: Products of magmatism or extensional tectonics?, *J. Geophys. Res.,95*, 4943-4965, 1990.

Blackman, D. K., and D. W. Forsyth, Isostatic compensation of tectonic features of the Mid-Atlantic Ridge: 25°-27°30'S, *J. Geophys. Res., 96*, 11,741-11,758, 1991.

Blackman, D.K., and D.W. Forsyth, The effects of plate thickening on three-dimensional, passive flow of the mantle beneath mid-ocean ridges, in *Mantle Flow and Melt Generation at Mid-Ocean Ridges, Geophys. Monogr. Ser.*, vol. 71, edited by J. Phipps Morgan, D.K.

Blackman, and J.M. Sinton, pp. 311-326, AGU, Washington, D.C., 1992.

Brace,W. F., and D. L. Kohlstedt, Limits on lithospheric stress imposed by laboratory experiments, *J. Geophys. Res., 85*, 6248-6252, 1980.

Buck, W. R., Flexural rotation of normal faults, *Tectonics, 7*, 959-973, 1988.

Buck, W.R., Effect of lithospheric thickness on the formation of high- and low-angle normal faults, *Geology, 21*, 933-936, 1993.

Carbotte, S. M., and K. C. Macdonald, The axial topographic high at intermediate and fast spreading centers, *Earth Planet. Sci. Lett., 128*, 85-97, 1994a.

Carbotte, S. M., and K. C. Macdonald, Comparison of seafloor tectonic fabric at intermediate, fast, and super fast spreading ridges: Influence of spreading rate, plate motions, and ridge segmentation on fault patterns, *J. Geophys. Res., 99*, 13,609-13,631, 1994b.

Chen, Y., Oceanic crustal thickness versus spreading rate, *Geophys. Res. Lett., 19,* 953-756, 1992.

Chen, Y., and W. J. Morgan, Rift valley/no rift valley transition at mid-ocean ridges, *J. Geophys. Res., 95*, 17,571-17,581, 1990a.

Chen, Y., and W. J. Morgan, A nonlinear rheology model for mid-ocean ridge axis topography, *J. Geophys. Res., 95*, 17,583-17,604, 1990b.

Cowie, P. A., and C. H. Scholz, Physical explanation for the displacement-length relationship for faults using a post-yield fracture mechanics model, *J. Struct. Geol., 14,* 1133-1148, 1992a.

Cowie, P. A., and C. H. Scholz, Displacement-length scaling relationship for faults: Data synthesis and discussion, *J. Struct. Geol., 14,* 1149-1156, 1992b.

Cowie, P. A., C. H. Scholz, M. Edwards, and A. Malinverno, Fault strain and seismic coupling on mid-ocean ridges, *J. Geophys. Res., 98*, 17,911-17,920, 1993.

Dawers, N. H., M. H. Anders, and C. H. Scholz, Growth of normal faults: Displacement-length scaling, *Geology, 21*, 1107-1110, 1993.

Detrick, R. S., R. S. White, and G. M. Purdy, Crustal structure of North-Atlantic fracture zones, *Rev. Geophys., 31*, 439-459, 1993.

Detrick, R. S., H. D. Needham, and V. Renard, Gravity anomaly and crustal thickness variations along the Mid-Atlantic Ridge between 33°N and 40°N, *J. Geophys. Res., 100*, 3767-3787, 1995.

Escartìn, J., and J. Lin, Ridge offsets, normal faulting, and gravity anomalies of slow spreading ridges, *J. Geophys. Res., 100*, 6163-6177, 1995.

Forsyth, D. W., Finite extension and low-angle normal faulting, *Geology, 20*, 27-30, 1992.

Goetze, C., The mechanisms of creep in olivine, *Philos. Trans. R. Soc. London, A, 288*, 99-119, 1978.

Goff, J. A., A global and regional stochastic analysis of near-ridge abyssal hill morphology, *J. Geophys. Res., 96,* 21,713-21,737, 1991.

Goff, J. A., B. E. Tucholke, J. Lin, G. E. Jaroslow, and M. C. Kleinrock, Quantitative analysis of abyssal hills in the Atlantic Ocean: A correlation between crustal thickness and extensional faulting, *J. Geophys. Res., 100*, 22,509-22,522, 1995.

Grindlay, N.R., P. J. Fox, and K. C. Macdonald, Second-order axis discontinuities in the South Atlantic: Morphology, structure, and evolution, *Mar. Geophys. Res., 13,* 21-50, 1991.

Huang, P. Y., S. C. Solomon, E. A. Bergman, and J. L. Nabelek, Focal depths and mechanisms of Mid-Atlantic Ridge earthquakes from body waveform inversion, *J. Geophys. Res., 91*, 579-578, 1986.

Ito, G., and J. Lin, Mantle temperature anomalies along the present and paleo-axes of the Galapagos spreading center as inferred from gravity analyses, *J. Geophys. Res., 100*, 3733-3745, 1995a.

Ito, G., and J. Lin, Oceanic spreading center-hot spot interactions: Constraints from along-isochron bathymetric and gravity anomalies, *Geology, 23*, 657-660, 1995b.

Karson, J. A., and H. J. B. Dick, Tectonics of ridge-transform intersections at the Kane Fracture Zone, *Mar. Geophys. Res., 6*, 51-98, 1983.

Kirby, S. H., Rheology of the lithosphere, *Rev. Geophys., 21*, 1458-1487, 1983.

Kuo, B.-Y., J. Phipps Morgan, and D. W. Forsyth, Asymmetry in topography of the crestal mountains near a ridge-transform intersection (abstract), *Eos Trans. AGU, 65*, 274, 1984.

Kuo, B.-Y., and D. W. Forsyth, Gravity anomalies of the ridge-transform system in the South Atlantic between 31° and 34.5°S: Upwelling centers and variations in crustal thickness, *Mar. Geophys. Res., 10*, 205-232, 1988.

Lee, S., and S. C. Solomon, Constraints from Sea Beam bathymetry on the development of normal faults on the East Pacific Rise, *Geophys. Res. Lett., 22*, 3135-3138, 1995.

Lin, J., and E. M. Parmentier, Mechanisms of lithospheric extension at mid-ocean ridges, *Geophys. J., 96*, 1-22, 1989.

Lin, J., and E.M. Parmentier, A finite amplitude necking model of rifting in brittle lithosphere, *J. Geophys. Res., 95*, 4909-4923, 1990.

Lin, J., and J. Phipps Morgan, The spreading rate dependence of three-dimensional mid-ocean ridge gravity structure, *Geophys. Res. Lett., 19*, 13-16, 1992.

Lin, J., G. M. Purdy, H. Schouten, J.-C. Sèmpère, and C. Zervas, Evidence from gravity data for focused magmatic accretion along the Mid-Atlantic Ridge, *Nature, 344*, 627-632, 1990.

Lin, J., B. E. Tucholke, and M. C. Kleinrock, Off-axis "boudin-shaped" gravity lows on the western flank of the Mid-Atlantic Ridge at 25°25'-27°10'N: Evidence for long-term pulses in magmatic accretion in spreading segments (abstract), *Eos Trans. AGU, 74(16)*, Spring Meet. suppl., 380, 1993.

Macdonald, K. C., Mid-ocean ridges: Fine scale tectonic, volcanic, and hydrothermal processes within the plate boundary zone, *Annu. Rev. Earth Planet. Sci., 10*, 155-190, 1982.

Macdonald, K. C., P. J. Fox, L. J. Perram, M. F. Eisen, R. M. Haymon, S. P. Miller, S. M. Carbotte, M.-H. Cormier, and A. N. Shaor, A new view of the mid-ocean ridge from the behavior ridge axis discontinuities, *Nature, 335,* 217-225, 1988.

Madsen J. A., R. S. Detrick, J. C. Mutter, P. Buhl, and J. A. Orcutt, A two- and three-dimensional analysis of gravity anomalies associated with the East Pacific Rise at 9°N and 13°N, *J. Geophys. Res., 95*, 14967-14987, 1990.

Malinverno, A., Inverse square-root dependance of mid-ocean-ridge flank roughness on spreading rate, *Nature, 352*, 58-60, 1991.

Menke, W., and D. Sparks, Crustal accretion model for Iceland predicts "cold" crust, *Geophys. Res. Lett., 22*, 1673-1676, 1995.

Minshull, T. A., E. Morris, and R. S. Detrick, Gravity anomalies and crustal structure at the Mesozoic Blake Spur Fracture Zone, *J. Geophys. Res., 100*, 17,771-17,779, 1995.

Morris, E., and R. S. Detrick, Three-dimensional analysis of gravity anomalies in the MARK area, Mid-Atlantic Ridge 23°N, *J. Geophys. Res., 96*, 4355-4366, 1991.

Neumann, G. A., and D. W. Forsyth, The paradox of the axial profile: Isostatic compensation along the axis of the Mid-Atlantic Ridge?, *J. Geophys. Res., 98*, 17,891-17,910, 1993.

Parmentier, E. M., and J. Phipps Morgan, Spreading rate dependence of three dimensional structure in oceanic spreading centers, *Nature, 348,* 325-328, 1990.

Phipps Morgan, J., and Y. J. Chen, The genesis of oceanic crust: Magma injection, hydrothermal circulation, and crustal flow, *J. Geophys. Res., 98*, 6283-6298, 1993.

Phipps Morgan, J., and D. W. Forsyth, Three-dimensional flow and temperature perturbations due to a transform offset: Effects on oceanic crustal and upper mantle structure, *J. Geophys. Res., 93*, 2955-2966, 1988.

Phipps Morgan, J., E. M. Parmentier, and J. Lin, Mechanisms for the origin of mid-ocean ridge axial topography: Implications for the thermal and mechanical structure of accreting plate boundaries, *J. Geophys. Res., 92*, 12,823-12,836, 1987.

Searle, R. C., and A. S. Laughton, Sonar studies of the Mid-Atlantic Ridge and Kurchatov Fracture Zone, *J. Geophys. Res., 82*, 5313-5328, 1977.

Searle, R. C., and A. S. Laughton, Fine-scale sonar study of tectonics and volcanism on the Reykjanes Ridge, *Oceanol. Acta, 4* suppl., 5-13, 1981.

Sempéré, J.-C., G. M. Purdy, and H. Schouten, Segmentation of the Mid-Atlantic Ridge between 24°N and 30°40'N, *Nature, 344*, 427-431, 1990.

Sempéré, J.-C., J. Lin, H.S. Brown, H. Schouten, and G.M. Purdy,

Segmentation and morphotectonic variations along a slow-spreading center: The Mid-Atlantic Ridge (24°N-30°40'N), *Mar. Geophys. Res.*, *9*, 153-200, 1993.

Severinghaus, J. P., and K. C. Macdonald, High inside corners at ridge-transform intersections, *Mar. Geophys. Res.*, *9*, 353-367, 1988.

Shaw, P.R., Ridge segmentation, faulting and crustal thickness in the Atlantic Ocean, *Nature, 358,* 490-493, 1992.

Shaw, P. R., and J. Lin, Causes and consequences of variations in faulting style at the Mid-Atlantic Ridge, *J. Geophys. Res.*, *98*, 21,839-21,851, 1993.

Shelton, G., and J. Tullis, Experimental flow laws for crustal rocks (abstract), *Eos Trans. AGU, 62(17)*, 396, 1981.

Sinha, M. C., and K. E. Louden, The Oceanographer fracture zone, I, Crustal structure from seismic refraction studies, *Geophys. J. R. Astron. Soc.*, *75*, 713-736, 1983.

Sleep, N. H., Formation of the oceanic crust: Some thermal constraints, *J. Geophys. Res.*, *80*, 4037-4042, 1975.

Smith, D. K., and J. R. Cann, The role of seamount volcanism in crustal construction at the Mid-Atlantic Ridge (24°-30°N), *J. Geophys. Res.*, *97*, 1645-1658, 1992.

Solomon, S. C., P. Y. Huang, and L. Meinke, The seismic moment budget of slowly spreading ridges, *Nature*, *334*, 58-60, 1988.

Sparks, D. W., E. M. Parmentier, and J. Phipps Morgan, Three-dimensional mantle convection beneath a segmented spreading center: Implications for along-axis variations in crustal thickness and gravity, *J. Geophys. Res., 98,* 21,977-21,995, 1993.

Thatcher, W., and D.P. Hill, A simple model for the fault-generated morphology of slow-spreading mid-ocean ridges, *J. Geophys. Res., 100,* 561-570, 1995.

Tolstoy, M. A., A. J. Harding, and J. A. Orcutt, Crustal thickness on the Mid-Atlantic Ridge: Bull's eye gravity anomalies and focused accretion, *Science, 262,* 726-729,1993.

Toomey, D. R., S. C. Solomon, G. M. Purdy, and M. H. Murray, Microearthquakes beneath median valley of Mid-Atlantic Ridge near 23°N: Hypocenters and focal mechanisms, *J. Geophys. Res., 90,* 5443-5458, 1985.

Toomey, D. R., S. C. Solomon, and G. M. Purdy, Microearthquakes beneath the median valley of the Mid-Atlantic Ridge near 23°N: Tomography and tectonics, *J. Geophys. Res., 93*, 9093-9112, 1988.

Tucholke, B. E., and J. Lin, A geological model for the structure of ridge segments in slow spreading crust, *J. Geophys. Res., 99*, 11,937-11,958, 1994.

Wang, X., and J. R. Cochran, Gravity anomalies, isostasy, and mantle flow at the East Pacific Rise, *J. Geophys. Res., 98*, 19,505-19,531, 1993.

White, R. S., D. McKenzie, and R. K. O'Nions, Oceanic crustal thickness from seismic measurements and rare earth inversions, *J. Geophys. Res., 97*, 19,683-19,715, 1992.

Wilson D. S., D. A. Clague, N. H. Sleep, and J. L. Morten, Implications of magma convection for the size and temperature of magma chamber at fast spreading ridges, *J. Geophys. Res., 93*, 11,974-11,984, 1988.

Zuber, M. T., E. M. Parmentier, and R. C. Fletcher, Extension of continental lithosphere: A model for two scales of Basin and Range deformation, *J. Geophys. Res., 91*, 4826-4838, 1986.

J. Lin and W.J. Shaw, Department of Geology and Geophysics, Woods Hole Oceanographic Institution, Woods Hole, MA 02543 (e-mail: jlin@whoi.edu; william@galileo.whoi.edu)

(Received October 31, 1995; revised March 18, 1996; accepted March 21, 1996.)